Boosting the Open Circuit Voltage and Fill Factor of QDSSCs Using Hierarchically Assembled ITO@Cu$_2$S Nanowire Array Counter Electrodes

Yan Jiang,[†] Bin-Bin Yu,[†] Jie Liu,[†] Zhi-Hua Li,[†] Jian-Kun Sun,[†] Xin-Hua Zhong,[‡] Jin-Song Hu,*[,†] Wei-Guo Song,*[,†] and Li-Jun Wan[†]

[†]Beijing National Laboratory for Molecular Sciences, Key Laboratory of Molecular Nanostructure and Nanotechnology, Institute of Chemistry, Chinese Academy of Sciences, 2 North First Street, Zhongguancun, Beijing 100190, China

[‡]Key Laboratory for Advanced Materials, Institute of Applied Chemistry, East China University of Science and Technology, Shanghai 200237, China

S *Supporting Information*

ABSTRACT: The key challenges in enhancing the power conversion efficiency (PCE) of a quantum dot-sensitized solar cell (QDSSC) are efficiently achieving charge separation at the photoanode and improving the charge transfer, which is limited by the interface between the electrolyte and the counter electrode (CE). Here, hierarchically assembled ITO@ Cu$_2$S nanowire arrays with conductive single-crystalline ITO cores and Cu$_2$S nanocrystal shells were designed as efficient QDSSCs CEs. These arrays not only provided an efficient three-dimensional charge transport network but also allowed for the effective deposition of more Cu$_2$S nanocrystals as active sites to catalyze the electrolyte reaction. This design considerably reduced the sheet and charge transfer resistance of the CE, thus decreasing the series resistance and increasing the shunt resistance of the QDSSC. As a result, QDSSCs with this CE exhibited an unprecedentedly high V_{oc} of 0.688 V, a fill factor of 58.39%, and a PCE of 6.12%, which is 21.2% higher than that of the conventional brass/Cu$_2$S CE.

KEYWORDS: Nanostructures, solar cells, quantum dots, charge transfer, three-dimensional
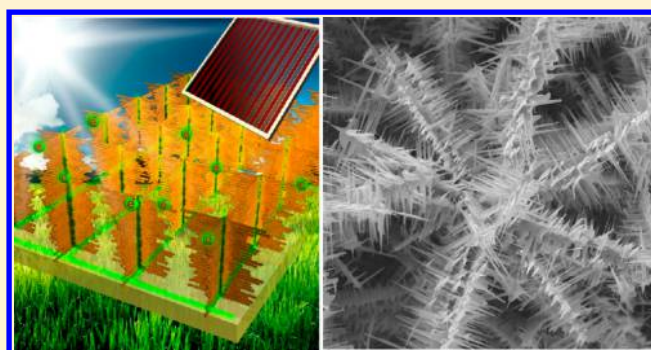
Dye-sensitized solar cells (DSSCs) have attracted significant attention in recent decades due to their relatively high power conversion efficiencies (PCE),[1−4] long stabilities,[5] and low-cost solution processing methods that significantly reduce the energy cost associated with solar cell manufacturing and therefore the energy payback time.[6−11] Quantum dot-sensitized solar cells (QDSSCs) are expected to overcome the shortcomings of DSSCs and achieve higher PCEs due to their many unique properties, including a tunable bandgap to match the full solar spectrum, multiple exciton generation, and hot carrier collection to multiply the current generation.[12−15] However, QDSSCs still lag far behind their predecessor, and the maximum thermodynamic conversion efficiency of 44% is not yet attainable. The best QDSSC PCE increased from less than 1% in 2002 to 5% in 2011.[16,17] Recently, with the development of the efficient loading of presynthesized quantum dots into photoanodes, QDSSCs with PCEs of up to 7% have been demonstrated.[18−20] However, the PCEs of QDSSCs need to be improved to at least 10% to stimulate scientific and industrial interest, and revitalize the field. To achieve this goal, intensive efforts should be focused on developing photoanodes with more efficient light absorption and faster electron injection, and counter electrodes (CEs) with better catalytic activity and faster charge transfer.

The overall PCE of a solar cell is determined by the product of the short circuit current (J_{sc}), open circuit voltage (V_{oc}), and fill factor (FF). For a QDSSC, the carrier generation and separation occur at the photoanode, but the charge transport is mainly limited by the interface between the electrolyte and the CE.[21] In addition to the development of photoanodes with more efficient light absorption and faster electron injection, the exploration of new CEs with enhanced S_n^{2-} to nS^{2-} reduction capabilities and enhanced charge transport is also critical to achieving high-efficiency QDSSCs.[22−26] Although it suffers from mechanical and chemical instability, the brass/Cu$_2$S CE remains the best CE.[27] Other options, such as FTO/Cu$_2$S CEs, result in either a low current density or a low fill factor.[28,29] Nanotechnology provides new opportunities to precisely control the morphologies and structures of CEs to increase the number of catalytic sites and engineer the interface between
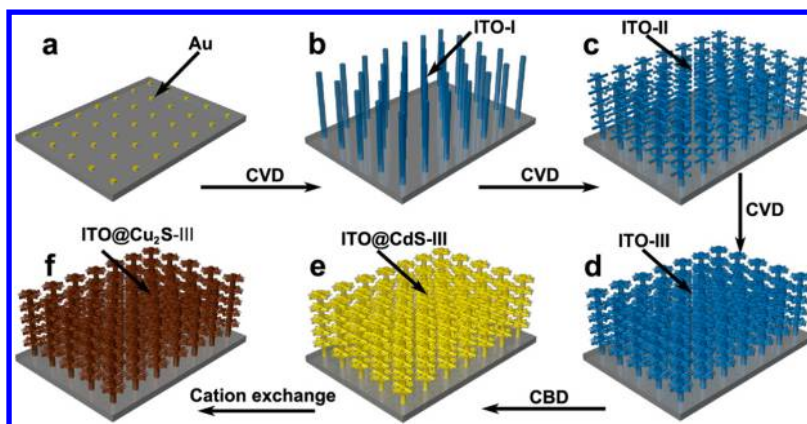
Figure 1. Schematic illustration of the fabrication of hierarchically assembled ITO@Cu$_2$S nanowire arrays on FTO. (a) The deposition of the gold catalysts on the FTO substrate. (b−d) The growth of ITO-I, ITO-II, and ITO-III via CVD. (e) The deposition of CdS shells on the ITO-III nanowire arrays via CBD. (f) The conversion of the CdS shells into Cu$_2$S shells via cation exchange to achieve the hierarchically assembled ITO@Cu$_2$S nanowire arrays.

the substrate and the catalyst to significantly improve the charge and mass transfer, and thus enhance the PCE of a QDSSC. Our recent work has demonstrated that ITO@Cu$_2$S core−shell nanowire arrays with high-quality tunnel junctions could be used as CEs with no stability issues; such nanowire arrays improve the performance of QDSSC by enhancing both J_{sc} and V_{oc}.[30] However, the FFs of the QDSSCs with previously designed ITO@Cu$_2$S CEs were still much lower than those with traditional brass/Cu$_2$S CEs, which limited the further enhancement of the PCE.[31]

As discussed in detail in the Supporting Information, the fill factor of a solar cell, which significantly influences its PCE, is closely related to its series resistance (R_s) and shunt resistance (R_{sh}) (Figure S1). It is generally reported that the counter electrode plays an important role in the charge flux in both DSSCs and QDSSCs. However, there are differences in this regard between these two types of solar cells, which is suggested by the differences in the shapes of their IV curves. The IV curve of a DSSC near the short circuit is commonly flatter than that of a state-of-the-art QDSSC, indicating that a larger R_{sh} can be easily achieved in DSSCs. R_{sh} is indicative of the efficiency of electron−hole separation compared with recombination. The larger R_{sh} indicates that the charge separaction in DSSCs is more efficient than in QDSSCs. Zaban et al. inverstigated this phenomenon and found that the inorganic QDs played a direct role in the recombination process.[32] The recombination process is much faster in QDSSCs than in DSSCs; thus, the R_{sh} can be influenced by the R_s in a QDSSC. A typical example is the difference in the performance and the corresponding R_{sh} and R_s of QDSSCs with FTO/Au and Cu$_2$S CEs. As shown in Figure S2 and Table S1, QDSSCs that use a brass/Cu$_2$S CE showed a much smaller R_s and a larger R_{sh} because the brass/Cu$_2$S CE exhibited a smaller sheet resistance (R_h) and larger transfer resistance (R_{ct}) than the FTO/Au CE.[30,31] It was believed that the improved charge transfer due to the decrease in the R_s alleviated the carrier recombination in the photoanode, which contributed the increase in the R_{sh}. Similar results have been found in a comparison of RGO-Cu$_2$S CEs and. Pts CE.[27] Therefore, the design of a QDSSC CE with a small R_s could facilitate the charge transfer at the interface between the electrolyte and the CE, which will reduce the charge recombination on the photoanode side and increase the R_{sh}. Moreover, the decrease

in the R_s will reduce the loss of photovoltage, and the increase in the R_{sh} will reduce the loss of photocurrent, both of which will lead to a high FF. Although several strategies, such as ZnS treatment, linker-assisted loading of quantum dots and control of the titania morphology, have been applied to photoanode preparation to improve charge separation and reduce charge recombination,[33−37] very few studies have focused on the precise design and control of the structure and morphology of a CE to reduce the R_s and increase the R_{sh} and thus enhance the PCE of a QDSSC. Here, hierarchically assembled nanowire arrays with conductive ITO cores and catalytically active Cu$_2$S nanocrystal shells were fabricated to effectively reduce the R_s and increase the R_{sh} of the QDSSCs. The hierarchically assembled ITO nanowire array not only provided a three-dimensional charge transport network but also allowed for the efficient deposition of Cu$_2$S to provide more active sites for catalyzing the reduction of S_n^{2-} to nS^{2-}. The formation of a tunnel junction at the high-quality ITO/Cu$_2$S interface considerably decreased the sheet and charge transfer resistance. Benefiting from the unique features of hierarchically assembled ITO@Cu$_2$S nanowire array as CEs, the QDSSC exhibited a high V_{oc} of 0.688 V, a high fill factor of 58.39%, and thus an enhanced PCE of 6.12%, which is 21.2% higher than that obtained using conventional brass/Cu$_2$S CEs.

Results and Discussion. The hierarchically assembled ITO@Cu$_2$S nanowire arrays were fabricated via the growth of hierarchically assembled ITO nanowire arrays using multistep chemical vapor deposition (CVD) followed by effectively coating Cu$_2$S nanocrystal shells onto the ITO nanowire cores. Briefly, as shown in Figure 1, a first-generation single-crystalline ITO nanowire array was grown on an FTO substrate via CVD using sputtered gold nanoparticles as catalysts (Figure 1a and b, ITO-I). The same process was repeated to grow the second-generation ITO nanowires (Figure 1c, ITO-II) on the ITO-I, which was followed by third-generation ITO nanowires (Figure 1d, ITO-III) grown on the ITO-II nanowires. A chemical bath deposition (CBD) was then performed to coaxially deposit a CdS layer on each ITO-III nanowire (Figure 1e), followed by cation exchange to finally achieve the hierarchically assembled nanowire array with ITO cores and Cu$_2$S nanocrystal shells (Figure 1f). The details are presented in the Experimental Section.
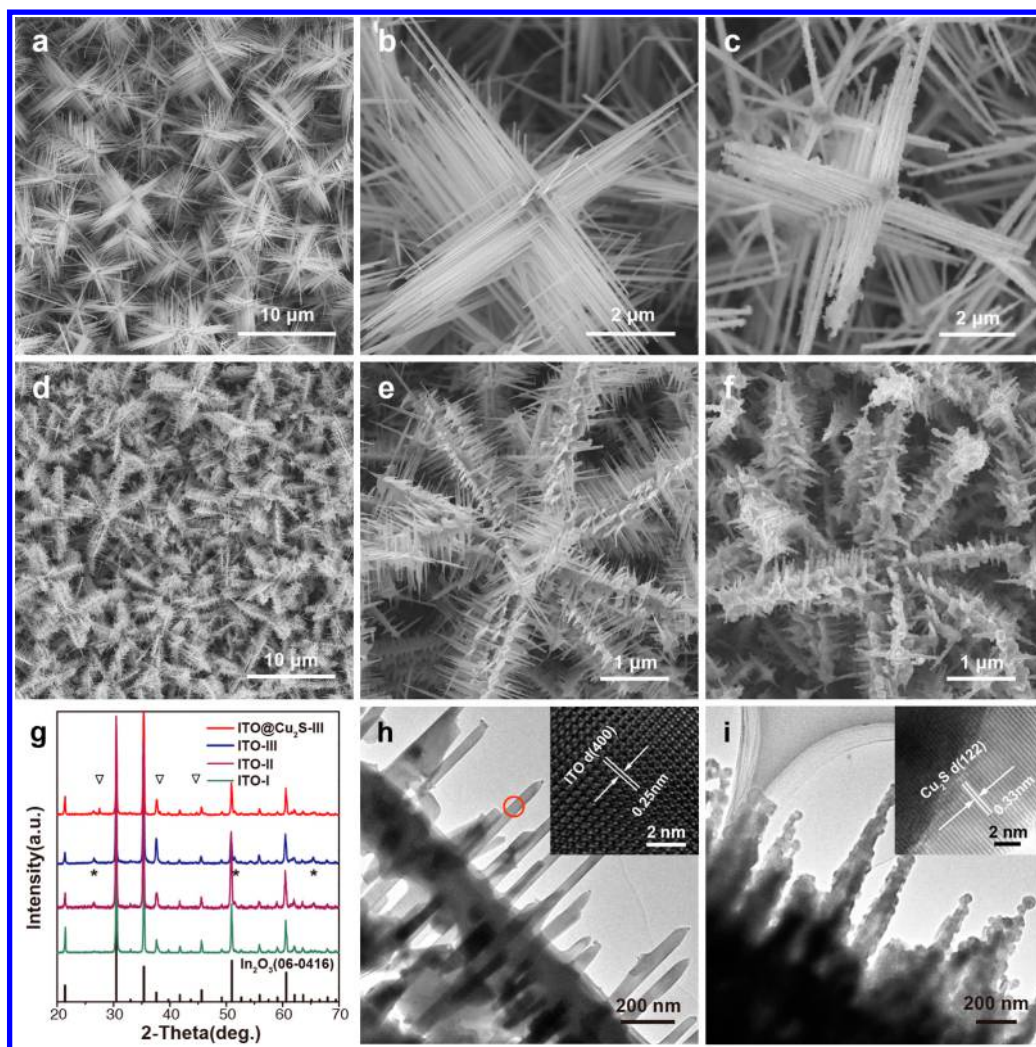
Figure 2. SEM images of hierarchical ITO nanowire arrays before and after the coaxial growth of the Cu$_2$S shell: (a) low- and (b) high-magnification SEM images of ITO-II. (c) SEM image of ITO@Cu$_2$S-II. (d) Low- and (e) high-magnification SEM images of ITO-III. (f) SEM image of ITO@ Cu$_2$S-III. (g) XRD patterns of In$_2$O$_3$ (JCPDS Card No. 06-0416) and ITO-I (green), ITO-II (purple), ITO-III (blue), and ITO@Cu$_2$S-III nanowires arrays (red). (h) TEM image of ITO-III nanowires. The inset shows an HRTEM image of the third-generation ITO branch marked by the red circle. (i) TEM image of ITO@Cu$_2$S-III nanowires. The inset shows an HRTEM image of a Cu$_2$S nanocrystal coated on a third-generation ITO branch.

The morphologies and structures of the ITO and ITO@ Cu$_2$S nanowire arrays were first investigated using scanning electron microscopy (SEM) and transmission electron microscopy (TEM). Figure 2a and b show typical low- and high-magnification SEM images of the ITO-II nanowire arrays. Four rows of nanowire branches were vertically grown on the surfaces of each ITO-I nanowire due to the square or rectangular cross-section, which results in four side facets (Figure S3). The smaller third-generation branches were sequentially grown on the surfaces of the second-generation branches via an additional CVD process, as shown in Figure 2d and e. The lengths of the second- and third-generation branches were controlled by the growth time. The crystalline structures of each generation of the nanowire array were characterized using X-ray diffraction (XRD). The diffraction peaks of each generation of the nanowire array shown in Figure 2g can be well indexed to cubic In$_2$O$_3$ (JCPDS Card No. 06-0416), except for the three peaks marked with stars at 26.6°, 51.8°, and 65.9° which can be attributed to diffraction on the (110), (211), and (301) crystallographic planes of SnO$_2$ (JCPDS Card No. 41-1445). These results indicate that the

nature of ITO did not change during the second- and the third-generation growth.

Moreover, after the CBD and cation exchange processes, the smooth surfaces of the ITO nanowire stems and branches became rough, and their diameters increased as shown in the SEM images (Figure 2c and f). The TEM image in Figure 2h shows third-generation branches with smooth surfaces, which were vertically grown on the second-generation branches. The continuous lattice fringes in the HRTEM image (inset in Figure 2h) show the single-crystalline nature of these branches. The distance of 0.25 nm is consistent with the d-spacing of the (400) crystallographic plane of ITO. After the growth of Cu$_2$S, the TEM image (Figure 2i) shows that the surfaces of the hierarchical ITO nanowire stems and branches were covered with nanoparticles. The HRTEM image (inset in Figure 2i) shows clear lattice fringes with a distance of 0.33 nm, which corresponds to the d-spacing of the (122) crystallographic plane of low-chalcocite Cu$_2$S. The typical XRD pattern of the ITO@Cu$_2$S-III nanowire arrays (red curve in Figure 2g) shows three additional peaks (marked with hollow inverted triangles) at 27.6°, 38.5°, and 44.8°, which can be attributed to diffraction
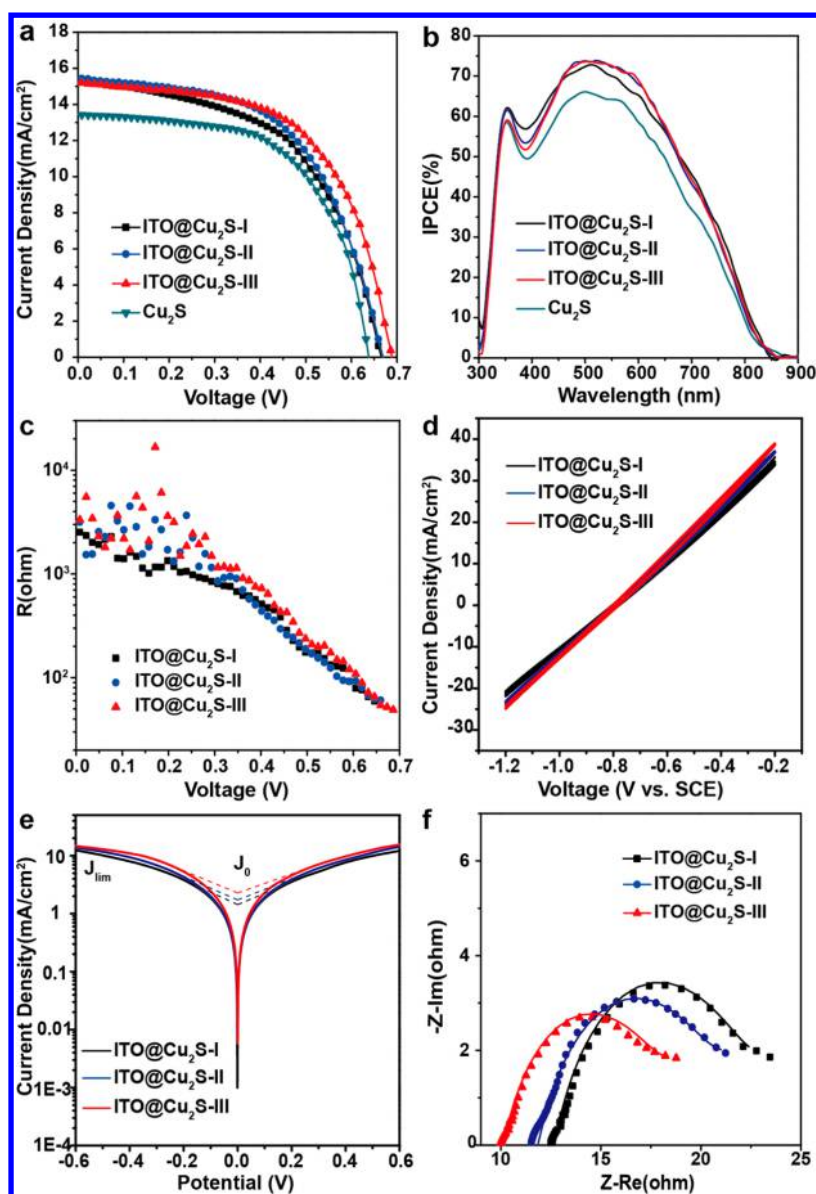
Figure 3. (a) Photocurrent−voltage curves and (b) IPCE spectra of the QDSSCs with the various ITO@Cu₂S and brass/Cu₂S CEs. (c) Resistance-voltage (R−V) curves of the QDSSCs with the various ITO@Cu₂S CEs. (d) Cyclic voltammograms of the various ITO@Cu₂S CEs. (e) Tafel polarization curves and (f) Nyquist plots from the EIS measurements of the various ITO@Cu₂S CEs recorded using symmetrical cells.

Table 1. Photovoltaic Parameters of the QDSSCs and the Resistances of Dummy Cells with Different CEs

counter electrode	V_{oc} (V)	J_{sc} (mA cm^{-2})	FF (%)	η (%)	R_s (Ω)	R_{sh} (Ω)	R_h (Ω)	R_{ct} (Ω cm^2)
ITO@Cu₂S-I	0.662	15.31	48.40	5.31	63.6	2865.1	6.29	1.87
ITO@Cu₂S-II	0.667	15.43	54.68	5.62	59.3	3988.7	5.93	1.44
ITO@Cu₂S-III	0.688	15.23	58.39	6.12	56.3	5399.2	5.05	1.30
brass/Cu₂S	0.638	13.42	58.90	5.05	54.7	7283.8		

from the (122), (240), and (204) crystallographic planes of low-chalcocite Cu₂S. X-ray photoelectron spectroscopy (XPS) corroborated the presence of Cu₂S, as indicated by the Cu(I) 2p and S 2p signals (Figure S4).

To evaluate the application of the hierarchical ITO@Cu₂S nanowire arrays as CEs in QDSSCs, the first-, second-, and third-generation ITO@Cu₂S nanowire arrays were used as CEs to fabricate QDSSCs and are designated ITO@Cu₂S-I, ITO@Cu₂S-II, and ITO@Cu₂S-III, respectively. The lengths of the ITO stems and branches in each CE as well as the thickness of

the Cu₂S nanocrystal shell were first optimized by changing the growth time. The length of the ITO nanowire stem and the second- and third-generation ITO branches used in the subsequent experiments were 8−10, 4−5, and 0.5−1 μm, respectively. The conventional brass/Cu₂S CE was used for comparison. The QDSSCs were fabricated using a CdSe$_x$Te$_{1-x}$-sensitized mesoporous TiO₂ photoanode, the above-mentioned four types of CEs, and a water/methanol (5:5, v/v)-based polysulfide electrolyte. It should be noted that there are ongoing debates in the literature about the use of methanol-

based electrolytes in QDSSCs. Klimov et al. recently reported a systematical analysis of the effect of methanol in the electrolyte on the performance of QDSSCs.[38] It was concluded that the enhancement of the device performance when using a methanol-containing electrolyte instead of pure water should be attributed to the improved contact between the QDs and the electrolyte due to the better wettability of methanol, rather than to methanol acting as a sacrificial donor. Therefore, the same water/methanol-based polysulfide electrolyte was used to fabricate all of the QDSSCs with the various CEs, including the brass/Cu$_2$S CE. Details for the fabrication of the photoanode and QDSSCs are provided in the Experimental Section. The photocurrent−voltage (J−V) curves of all QDSSCs are shown in Figure 3a, and the corresponding data are listed in Table 1. The QDSSCs with the ITO@Cu$_2$S nanowire CEs exhibited higher current densities and open circuit voltages than the QDSSC with the brass/Cu$_2$S CE. The monochromatic incident photon-to-electron conversion efficiency (IPCE) measurements in Figure 3b show increases of nearly 10% in the IPCE between the wavelengths of 450−700 nm for the QDSSCs with ITO@Cu$_2$S CEs compared with the QDSSC with the brass/Cu$_2$S CE. These results indicate that the increase in J_{sc} could be attributed to the improved utilization efficiency of the incident light due to the light scattering caused by the three-dimensional nanowire array structure in the ITO@Cu$_2$S CEs. Slight differences in J_{sc} and IPCE were observed among the QDSSCs with the three types of ITO@Cu$_2$S CEs. Because our previous results showed that the transmittances of ITO nanowire arrays over 10 μm were very similar in the spectral range of 300−850 nm and close to 0%,[30] the significant difference in the scattering effect of the light in the range of ~350−850 nm for the three types of ITO@Cu$_2$S CEs was not expected. Moreover, all QDSSCs with ITO@Cu$_2$S CEs exhibited a higher V_{oc} than that with the brass/Cu$_2$S CE. The V_{oc} increased from 0.662 V for the ITO@Cu$_2$S-I CE, to 0.667 V for the ITO@Cu$_2$S-II CE and to 0.688 V for the ITO@Cu$_2$S-III CE, which is one of the highest V_{oc} achieved among reported QDSSCs.[39] It should be noted that the fill factor was appreciably increased by 20.6%, from 48.40% to 58.39%, after the introduction of the hierarchically assembled structures. As a result, the total PCE reached 6.12% for the QDSSC with the ITO@Cu$_2$S-III CE, corresponding to 15.3% and 21.2% increases compared to the QDSSC with the ITO@Cu$_2$S-I CE and the brass/Cu$_2$S CE, respectively.

To understand the notable increase in the fill factor and V_{oc} of the QDSSC with the ITO@Cu$_2$S-III CE, the R_s and R_{sh} were estimated according to the following eq 1:

$$R = -\left(\frac{dJ}{dV}\right)^{-1} \tag{1}$$

The resistance−voltage (R−V) curves were derived from the IV curves as shown in Figure 3c. The resistances close to the short and open circuit in the R−V curves are represented by R_{sh} and R_s, respectively.[33] It can be seen that the R_s decreased progressively while the R_{sh} increased appreciably from ITO@Cu$_2$S-I, to ITO@Cu$_2$S-II, and to ITO@Cu$_2$S-III. This result is consistent with the values simulated by the Oriel test station and listed in Table 1. The R_s decreased from 63.6 to 53.6 Ω and the R_{sh} increased from 2865.1 to 5399.2 Ω after the introduction of the hierarchically assembled structures in ITO@Cu$_2$S-III. As discussed in the Supporting Information, the decrease in the R_s will reduce the loss of the photovoltage,

and the increase in the R_{sh} will reduce the loss of photocurrent, both of which will contribute to the increase in the fill factor. Moreover, the increase in the R_{sh} will cause an increase in the V_{oc} according to the following eq 2:

$$\frac{V_{oc}}{R_{sh}} = I_L - I_0\left(\exp\left(\frac{qV_{oc}}{nkT}\right) - 1\right) \tag{2}$$

where I_L, I_0, n, q, k, and T are the light generated current, diode saturation current, ideality factor, elementary charge, Boltzmann constant, and temperature, respectively. These results are consistent with the measured values for the different ITO@Cu$_2$S CEs, as listed in Table 1. A nearly 50 mV increase in the V_{oc} was observed in the case of the ITO@Cu$_2$S-III CE compared with the brass/Cu$_2$S CE. Given that the same photoanode and device structure were used in these two cells, it was reasonably assumed that the hierarchical three-dimensional morphology of the ITO@Cu$_2$S-III CE benefited the light scattering and thus the light absorption on the photoanode side. This result is in good agreement with the increase in the IPCE response and photocurrent. It should be noted that the increase in the light generated current would generally cause the increase in the V_{oc} according to eq 3:

$$V_{oc} = \frac{nkT}{q}\ln\left(\frac{I_L}{I_0} + 1\right) \tag{3}$$

Therefore, the QDSSC with the ITO@Cu$_2$S-III CE showed an increased V_{oc} compared with the QDSSC with the brass/Cu$_2$S CE.

To evaluate the catalytic activity of the various ITO@Cu$_2$S CEs, cyclic voltammetry measurements were performed to elucidate the redox processes on the catalysts. Figure 3d shows the cyclic voltammograms of the various ITO@Cu$_2$S CEs recorded with a three-electrode system. The same polysulfide electrolyte was used as in the QDSSCs. The cycling was performed 10 times at a scan rate of 50 mV/s. Little change was observed in the curve shape or current density after 10 cycles, demonstrating the high chemical stability of the ITO@Cu$_2$S CEs. The highest current density at reductive potentials was achieved for the ITO@Cu$_2$S-III CE, confirming that it has the best catalytic activity for the reduction S_n^{2-} to nS^{2-}. A Tafel polarization measurement was further conducted on the various ITO@Cu$_2$S CEs to investigate the charge transfer kinetics using symmetrical cells consisting of two identical CEs and the electrolyte (Figure 3e). The extrapolated intercepts of the anodic and cathodic branches of the Tafel polarization curves indicate the exchange current density (J_0). A larger slope can be observed for ITO@Cu$_2$S-III compared with ITO@Cu$_2$S-I and ITO@Cu$_2$S-II, revealing a higher J_0 on the electrode. Because J_0 is inversely proportional to R_{ct} according to the following eq 4:

$$J_0 = \frac{RT}{nFR_{ct}} \tag{4}$$

where R is the gas constant, T is the temperature, n is the number of electrons involved in the reaction, and F is the Faraday's constant. The smallest R_{ct} was achieved for the ITO@Cu$_2$S-III CE, indicating that it had the best catalytic activity. Moreover, the limited current density (J_{lim}), which is related to the diffusion velocity of the ionic carrier in the polysulfide electrolyte and the catalytic properties of the CE, can also be deduced from the Tafel polarization curves. J_{lim} slightly increased after the introduction of the hierarchically assembled

ITO nanowire arrays. According to eq 5, the increase in J_{lim} implies that a larger diffusion coefficient (D) for polysulfide was achieved for the ITO@Cu$_2$S-III CE:

$$J_{lim} = \frac{2ncFD}{l} \tag{5}$$

where c is the polysulfide concentration and l is the spacer thickness.[25] A faster diffusion of the polysulfide electrolyte could reduce the R_s and thus increase the R_{sh} by reducing the electron−hole recombination within the photoanode, which is consistent with the results of the $R−V$ curves.

Furthermore, the sheet resistance of the CE and the charge transfer resistance at the interface between the CE and the electrolyte were analyzed using electrochemical impedance spectroscopy (EIS) measurements on the symmetrical cells. The modeled suitable equivalent circuits are shown in Figure S5 of the Supporting Information. The EIS spectra in Figure 3f and the data in Table 1 show that all of the ITO@Cu$_2$S nanowire array CEs exhibited relatively small R_h and R_{ct} (several ohms) at the solid/liquid interface. The small R_h could be attributed to the highly degenerate semiconductor nature of the synthesized ITO nanowires. The small R_{ct} should be attributed to the efficient electron and mass transfer in the three-dimensional nanowire array as well as to the formation of an effective tunneling junction between the n-type degenerate ITO nanowires and the p-type degenerate Cu$_2$S nanocrystals.[30] Compared with the original ITO@Cu$_2$S-I nanowire array CEs, the second-generation hierarchically branched ITO@Cu$_2$S-II CE exhibited lower R_h and R_{ct}, which could be further reduced upon the introduction of third-generation ITO branches (ITO@Cu$_2$S-III). The decrease in R_h from 6.29 Ω for ITO@Cu$_2$S-I to 5.05 Ω for ITO@Cu$_2$S-III could be attributed to the formation of conductive networks in the hierarchically branched nanowire arrays, which facilitated charge transfer within the electrode. This result is consistent with the decrease in the film resistances from ITO-I to ITO-III measured using a four-probe resistivity setup (Table S2). In contrast, R_{ct} decreased from 1.87 Ω cm^2 for ITO@Cu$_2$S-I to 1.30 Ω cm^2 for ITO@Cu$_2$S-III, which is in good agreement with the result from the analysis of the Tafel curves. This decrease is attributable to the increase in the contact area between Cu$_2$S and the electrolyte in terms of the more efficient loading of Cu$_2$S nanocrystals in the hierarchically branched nanowire arrays compared to the nonbranched nanowire arrays. The decreases in both R_h and R_{ct} contributed to the decrease in R_s, which facilitated charge transfer during the operation of the QDSSC and, consequently, decreased the charge recombination and increased the V_{oc} and PCE.

Stability is important when evaluating a counter electrode. Our previous results showed that a set of QDSSCs sequentially assembled with the same ITO@Cu$_2$S-I CE exhibited almost the same performance in terms of similar photovoltaic parameters. The morphology of the CE was nearly unchanged before and after assembling a set of QDSSCs.[31] To evaluate the long-term stability of the newly designed ITO@Cu$_2$S-III CE, a symmetrical cell was assembled with two ITO@Cu$_2$S-III CEs and the polysulfide electrolyte. Continuous potential sweeping was conducted for 300 cycles at a scan rate of 100 mV/s to evaluate the current−potential response. As shown in Figure 4, a very small current drop was observed after 300 cycles of continuous potential sweeping. This result is much better than that of some CEs reported in the literature, such as Cu$_x$S ($x > 1.75$) CEs,[24]
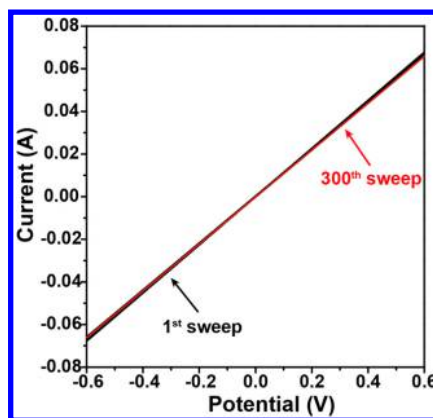

Figure 4. Stability test of the ITO@Cu$_2$S-III CE by continuous potential sweeping of the symmetrical cell.

indicating that the present ITO@Cu$_2$S-III CE could be used as a stable and reliable CE in QDSSCs.

Conclusion. A programmable, hierarchically branched ITO@Cu$_2$S nanowire array was designed and fabricated as a novel, efficient counter electrode for QDSSCs that exhibited excellent performance with a high activity and good stability. Because the branched ITO@Cu$_2$S CE enhanced the utilization efficiency of the incident light and contributed to the decrease in R_s and the increase in R_{sh}, QDSSCs with this type of CE exhibited enhanced V_{oc} and FFs, resulting in a PCE of 6.12%. It was also interesting that precise nanostructuring of the counter electrode could not only reduce the R_s but also increase the R_{sh} of a QDSSC; these changes result in a significant enhancement of its PCE. This concept could inspire the development of new nanostructures for counter electrodes, further improving the PCE of QDSSCs and encouraging progress in the photoanode field.

Experimental Section. *Synthesis of Hierarchical ITO Nanowire Arrays.* FTO glass (14 Ω/□, Nippon Sheet Glass, S″MET China) was used as the substrate and cleaned by sequentially sonicating in water, ethanol, and acetone, followed by O$_2$ plasma treatment (PJ, AST, USA) for 15 min. The CVD process was performed to grow the ITO nanowires under an airflow of 1.5 sccm using sputtered gold particles as catalysts and metallic indium and tin powders (99.99%, Sigma-Aldrich) in a weight ratio of 10:1 as the source materials. The source temperature was maintained at 800 °C, and the chamber pressure was maintained at 30 Pa. The hierarchical ITO nanowire arrays were prepared by repeating the above procedure two times (ITO-II) or three times (ITO-III). In a typical procedure for the growth of the third-generation hierarchical ITO nanowire arrays, the gold catalysts were sequentially deposited with thicknesses of 10, 8, and 5 nm in each step, and the growth times were 20, 15, and 5 min, respectively. The lengths of the ITO nanowire stems and second- and third-generation ITO branches used in the subsequent experiments were 8−10 μm, 4−5 μm, and 0.5−1 μm, respectively.

Synthesis of the ITO@Cu$_2$S Nanowire Arrays. The ITO-I, ITO-II, and ITO-III nanowire arrays on the FTO substrate were placed into a flask containing 22 mL of 15 mM CdSO$_4$. An NH$_4$OH aqueous solution (28 mL of NH$_4$OH in 150 mL of DI water) was then added to adjust the pH. When the solution temperature rose to 65 °C, 22 mL of a 0.75 M thiourea solution was added to induce the reaction for 11 min. The substrate was

then thoroughly washed with DI water. Then, the yellowish substrate with the CdS coating was immersed in 0.5 M CuCl at 50 °C for 30 min to achieve the complete conversion of CdS into Cu_2S.

Preparation of the Counter Electrodes. The ITO-I@Cu_2S, ITO-II@Cu_2S, and ITO-III@Cu_2S nanowire arrays were calcinated at 300 °C for 30 min under Ar atmospheres to improve the crystallinity and junction quality and were then directly used as counter electrodes in the QDSSCs.

Preparation of the Photoanodes. A $CdSe_xTe_{1-x}$-sensitized TiO_2 photoanode was prepared according to the literature.[18] Briefly, commercial P25 TiO_2 nanoparticles (Degussa) were used to fabricate a 12 μm translucent TiO_2 film on the FTO substrate, followed by coating with a 4-μm-thick TiO_2 scattering layer (200 nm) via a screen printing method. $CdSe_xTe_{1-x}$ quantum dots (QDs) of ∼6 nm were prepared via the hot injection method followed by ligand exchange to obtain 3-mercaptopropionic acid (MPA)-capped water-soluble quantum dots. The typical TEM image, normalized absorbance and PL emission spectra of the $CdSe_xTe_{1-x}$ quantum dots were shown in Figures S6 and S7, respectively. For each photoanode, 30 μL of an aqueous MPA-capped QD solution was pipetted, and the immobilization procedure was maintained for 7 h before sequentially rinsing with water and ethanol. A ZnS treatment was performed by alternately dipping the photoanode twice into 0.1 M $Zn(OAc)_2$ and 0.1 M Na_2S solutions for 1 min and then drying before use. A cross-sectional SEM image of the $CdSe_xTe_{1-x}$-sensitized photoanode was presented in Figure S8.

Preparation of the QDSSCs. The QDSSCs were fabricated by using the $CdSe_xTe_{1-x}$-sensitized TiO_2 photoanodes, a polysulfide electrolyte, and the ITO-I@Cu_2S, ITO-II@Cu_2S, ITO-III@Cu_2S nanowire arrays as well as conventional brass/Cu_2S as counter electrodes. The brass/Cu_2S counter electrodes was prepared according to the literature.[40] The polysulfide electrolyte was prepared using 1 M sulfur, 1 M Na_2S and 0.2 M KCl in water/methanol (5:5, v/v). 3 M adhesive tape with a thickness of approximately 50 μm was used as a spacer to encapsulate the electrolyte between the photoanode and the counter electrodes.

Characterization. Field emission scanning electron microscopy (JSM 6701, JEOL, Japan) and transmission electron microscopy (JEM 2100F, JEOL, Japan) were used to characterize the morphologies and compositions of all of the materials. XRD experiments were performed on a Rigaku D/max-2500 diffractometer. A potentiostat (PARSTAT 2273A, Princeton Applied Research) was used to perform electrochemical impedance spectroscopy measurements.

Photovoltaic Measurements. A solar simulator (450 W, model 91150, Newport) with an AM 1.5 spectral distribution was used as the irradiation source and calibrated against an NREL reference cell to accurately simulate one full-sun intensity (100 mW/cm^2). All IPCE tests were performed on an IQE-200 measurement system with a motorized 1/8 m monochromator (model 74000, Newport) in the DC mode. A copper mask with a 0.16 cm^2 window was clipped on the photoanode side of the sandwiched QDSSC to define the active area.

ASSOCIATED CONTENT

$\circ$ Supporting Information

Discussion of the effects of the shunt and series resistances on the fill factor, photocurrent–voltage curves of QDSSCs with Au and Cu_2S CEs, SEM image of ITO-I nanowires, XPS analysis of hierarchically assembled ITO@Cu_2S-III nanowires, equivalent circuit for fitting the EIS of the ITO@Cu_2S CEs, TEM image of the $CdSe_xTe_{1-x}$ quantum dots, normalized absorbance and PL emission spectra of the $CdSe_xTe_{1-x}$ quantum dots, cross-sectional SEM image of the $CdSe_xTe_{1-x}$-sensitized photoanode, and film resistances of the three types of ITO nanowire arrays. The Supporting Information is available free of charge on the ACS Publications website at DOI: 10.1021/acs.nanolett.5b00096.

AUTHOR INFORMATION

Corresponding Authors
*E-mail: hujs@iccas.ac.cn.
*E-mail: wsong@iccas.ac.cn.

Notes
The authors declare no competing financial interest.

REFERENCES

(1) Yella, A.; Lee, H.; Tsao, H. N.; Yi, C.; Chandiran, A. K.; Nazeeruddin, M. K.; Diau, E. W.; Yeh, C.; Zakeeruddin, S. M.; Grätzel, M. *Science* **2011**, *334*, 629−634.

(2) Mathew, S.; Yella, A.; Gao, P.; Humphry-Baker, R.; Curchod, B. F. E.; Ashour, S. S.; Tavernelli, I.; Rothlisberger, U.; Nazeeruddin, M. K.; Grätzel, M. *Nat. Chem.* **2014**, *6*, 242−247.

(3) Law, M.; Greene, L. E.; Johnson, J. C.; Saykally, R.; Yang, P. *Nat. Mater.* **2005**, *4*, 455−459.

(4) Cui, J.; Lu, J.; Xu, X.; Cao, K.; Wang, Z.; Alemu, G.; Yuang, H.; Shen, Y.; Xu, J.; Cheng, Y.; Wang, M. *J. Phys. Chem. C* **2014**, *118*, 16433−16440.

(5) Joly, D.; Pelleja, L.; Narbey, S.; Oswald, F.; Chiron, J.; Clifford, J. N.; Palomares, E.; Demadrille, R. *Sci. Rep.* **2014**, *4*, 4033.

(6) Chu, L.; Li, L.; Su, J.; Tu, F.; Liu, N.; Gao, Y. *Sci. Rep.* **2014**, *4*, 4420.

(7) Luo, J.; Xu, M.; Li, R.; Huang, K. W.; Jiang, C.; Qi, Q.; Zeng, W.; Zhang, J.; Chi, C.; Wang, P.; Wu, J. *J. Am. Chem. Soc.* **2014**, *136*, 265−272.

(8) Song, W.; Vannucci, A. K.; Farnum, B. H.; Lapides, A. M.; Brennaman, M. K.; Kalanyan, B.; Alibabaei, L.; Concepcion, J. J.; Losego, M. D.; Parsons, G. N.; Meyer, T. J. *J. Am. Chem. Soc.* **2014**, *136*, 9773−9779.

(9) Wu, W.; Xu, Y.; Rao, H.; Su, C.; Kuang, D. *J. Am. Chem. Soc.* **2014**, *136*, 6437−6445.

(10) Jeanbourquin, X. A.; Li, X.; Law, C.; Barnes, P. R.; Humphry-Baker, R.; Lund, P.; Asghar, M. I.; O'Regan, B. C. *J. Am. Chem. Soc.* **2014**, *136*, 7286−7294.

(11) Pascoe, A. R.; Huang, F.; Duffy, N. W.; Cheng, Y. *J. Phys. Chem. C* **2014**, *118*, 15154−15161.

(12) Robel, I.; Subramanian, V.; Kuno, M.; Kamat, P. V. *J. Am. Chem. Soc.* **2006**, *128*, 2385−2393.

(13) Kamat, P. V. *J. Phys. Chem. C* **2008**, *112*, 18737−18753.

(14) Plass, R.; Pelet, S.; Krueger, J.; Grätzel, M. *J. Phys. Chem. B* **2002**, *106*, 7578−7580.

(15) Tian, J.; Lv, L.; Fei, C.; Wang, Y.; Liu, X.; Cao, G. *J. Mater. Chem. A* **2014**, *2*, 19653−19659.

(16) McDaniel, H.; Fuke, N.; Pietryga, J. M.; Klimov, V. I. *J. Phys. Chem. Lett.* **2013**, *4*, 355−361.

(17) Zhang, Q.; Guo, X.; Huang, X.; Huang, S.; Li, D.; Luo, Y.; Shen, Q.; Toyoda, T.; Meng, Q. *Phys. Chem. Chem. Phys.* **2011**, *13*, 4659−4667.

(18) Pan, Z.; Zhao, K.; Wang, J.; Zhang, H.; Feng, Y.; Zhong, X. *ACS Nano* **2013**, *7*, 5215−5222.

(19) Wang, J.; Mora-Sero, I.; Pan, Z.; Zhao, K.; Zhang, H.; Feng, Y.; Yang, G.; Zhong, X.; Bisquert, J. *J. Am. Chem. Soc.* **2013**, *135*, 15913−15922.

(20) Pan, Z.; Mora-Sero, I.; Shen, Q.; Zhang, H.; Li, Y.; Zhao, K.; Wang, J.; Zhong, X.; Bisquert, J. *J. Am. Chem. Soc.* **2014**, *136*, 9203−9210.

(21) Kamat, P. V.; Christians, J. A.; Radich, J. G. *Langmuir* **2014**, *30*, 5716−5725.

(22) Yang, Y.; Zhu, L.; Sun, H.; Huang, X.; Luo, Y.; Li, D.; Meng, Q. *ACS Appl. Mater. Interfaces* **2012**, *4*, 6162−6168.

(23) Parand, P.; Samadpour, M.; Esfandiar, A.; Zad, A. I. *ACS Photonics* **2014**, *1*, 323−330.

(24) Kim, C. S.; Choi, S. H.; Bang, J. H. *ACS Appl. Mater. Interfaces* **2014**, *6*, 22078−22087.

(25) Liu, F.; Zhu, J.; Hu, L.; Zhang, B.; Yao, J.; Nazeeruddin, M. K.; Grätzel, M.; Dai, S. *J. Mater. Chem. A* **2015**, *3*, 6315−6323.

(26) Park, J.-H.; Kang, S.-J.; Kim, S.; Lee, H.; Lee, J.-S. *RSC Adv.* **2014**, *4*, 51471−51476.

(27) Radich, J. G.; Dwyer, R.; Kamat, P. V. *J. Phys. Chem. Lett.* **2011**, *2*, 2453−2460.

(28) Ye, M.; Chen, C.; Zhang, N.; Wen, X.; Guo, W.; Lin, C. *Adv. Energy Mater.* **2014**, *4*, 1301564.

(29) Zhao, K.; Yu, H.; Zhang, H.; Zhong, X. *J. Phys. Chem. C* **2014**, *118*, 5683−5690.

(30) Jiang, Y.; Zhang, X.; Ge, Q.; Yu, B.; Zou, Y.; Jiang, W.; Song, W.; Wan, L.; Hu, J. *Nano Lett.* **2014**, *14*, 365−372.

(31) Jiang, Y.; Zhang, X.; Ge, Q.; Yu, B.; Zou, Y.; Jiang, W.; Hu, J.; Song, W.; Wan, L. *ACS Appl. Mater. Interfaces* **2014**, *6*, 15448−15455.

(32) Hod, I.; González-Pedro, V.; Tachan, Z.; Fabregat-Santiago, F.; Mora-Seró, I.; Bisquert, J.; Zaban, A. *J. Phys. Chem. Lett.* **2011**, *2*, 3032−3035.

(33) Yan, K.; Chen, W.; Yang, S. *J. Phys. Chem. C* **2013**, *117*, 92−99.

(34) Toyoda, T.; Shen, Q. *J. Phys. Chem. Lett.* **2012**, *3*, 1885−1893.

(35) Guijarro, N.; Campina, J. M.; Shen, Q.; Toyoda, T.; Lana-Villarreal, T.; Gomez, R. *Phys. Chem. Chem. Phys.* **2011**, *13*, 12024−12032.

(36) Prasittichai, C.; Hupp, J. T. *J. Phys. Chem. C* **2010**, *1*, 1611−1615.

(37) de la Fuente, M. S.; Sánchez, R. S.; González-Pedro, V.; Boix, P. P.; Mhaisalkar, S. G.; Rincón, M. E.; Bisquert, J.; Mora-Seró, I. *J. Phys. Chem. Lett.* **2013**, *4*, 1519−1525.

(38) McDaniel, H.; Fuke, N.; Makarov, N. S.; Pietryga, J. M.; Klimov, V. I. *Nat. Commun.* **2013**, *4*, 2887.

(39) Toyoda, T.; Shen, Q. *J. Phys. Chem. Lett.* **2012**, *3*, 1885−1893.

(40) Gonzalez-Pedro, V.; Xu, X.; Mora-Sero, I.; Bisquert, J. *ACS Nano* **2010**, *4*, 5783−5790.